

Fractional-order modeling and numerical simulation of diphtheria transmission in Rohingya refugee settlements using the fractional Adams-Bashforth-Moulton method

Md Nurul Raihen^{†*}, Md Abdul Kadir[‡], Vinodh Chellamuthu[§], Mansoor Alsulami^{**}

[†]Department of Mathematics and Statistics, University of Toledo, OH, 43607, USA

[‡]Department of Mathematics, University of Houston, TX, 77204, USA

[§]Department of Mathematics, Utah Tech University, UT, 84770, USA

^{**}Department of Mathematics, King Abdulaziz University, Jeddah, 21589, Saudi Arabia

Email(s): nurul.raihen@gmail.com, farhad.kadir@gmail.com, vinodh.chellamuthu@utahtech.edu, maalsulami2@kau.edu.sa

Abstract. Fractional order derivatives have become increasingly significant in mathematical modeling of infectious disease dynamics due to their ability to capture memory and hereditary properties of biological processes. In this study, we adopt and analyze a fractional order susceptible-latent-infectious-recovered model to investigate the spread of diphtheria among the Rohingya refugee population in Bangladesh. The model incorporates the Caputo definition of the fractional derivative and is solved numerically using the Fractional Adams-Bashforth-Moulton method (FABMM). Model parameters, including disease transmission and recovery rates, are estimated using available epidemiological data. The impact of varying the fractional order and other key parameters on the progression and control of the outbreak is explored through comprehensive numerical simulations. Graphical representations of daily and cumulative case trajectories for different fractional orders are presented, highlighting the effectiveness of fractional modeling in forecasting and controlling outbreaks. The results suggest that fractional order models provide more flexible and realistic predictions compared to classical integer-order approaches. These findings can aid the Bangladeshi government and humanitarian organizations in developing effective disaster response and public health strategies for preventing and managing diphtheria outbreaks.

Keywords: Mathematical modeling, epidemiology, fractional calculus, Caputo sense, FABMM

AMS Subject Classification 2020: 34A08, 34K37.

*Corresponding author

Received: 18 October 2025/ Revised: 27 December 2025/ Accepted: 08 January 2026

DOI: [10.22124/jmm.2026.31992.2892](https://doi.org/10.22124/jmm.2026.31992.2892)

1 Introduction

Infectious diseases arise from pathogenic microorganisms such as bacteria, viruses, and parasites, and are transmitted through respiratory emissions, direct contact, or exposure to contaminated biological fluids, including feces and blood [23]. Despite significant advances in modern medical technologies, humanity remains vulnerable to these life-threatening microorganisms. The COVID-19 pandemic brought into sharp focus the extent of our collective vulnerability [15]. The practical relevance of epidemiology has drawn considerable attention from researchers within mathematical biology. Real-time modeling enables the extraction of critical insights into epidemic dynamics [22], including resource requirements and the fundamental mechanisms of disease transmission, thereby supporting informed decision-making for future interventions [12].

Diphtheria is a highly contagious respiratory illness caused by *Corynebacterium diphtheriae* and is predominantly transmitted via airborne droplets. Effective prevention is achievable through widespread immunization programs, which have significantly reduced its global incidence. Active surveillance, including the identification and isolation of symptomatic individuals, plays a critical role in limiting transmission. Clinical manifestations often include fever, fatigue, sore throat, and cervical lymphadenopathy, while severe cases may involve toxin-mediated damage to vital organs such as the heart and kidneys, potentially resulting in respiratory failure, cardiac arrest, or death [14].

A severe diphtheria outbreak occurred in the overcrowded refugee camp of Southern Bangladesh in November 2017. By the end of 2019, the cumulative number of reported cases reached 7,064, with only 4% laboratory-confirmed [21]. Over the past few decades, the Rohingya population has endured repeated forced displacement, leading many to live as refugees in Bangladesh. In August 2017, approximately 625,000 Rohingyas fled Myanmar and settled in the largest refugee camp in Bangladesh [24]. Chronic undernutrition, coupled with limited access to healthcare, has made the camp highly susceptible to recurrent outbreaks of infectious diseases, including diarrhea, malaria, dengue, measles, and chikungunya [13].

Despite limited outbreak control measures in certain regions, many researchers have sought to understand the transmission dynamics of diphtheria and develop effective strategies for disease mitigation. Mathematical modeling in epidemiology has emerged as a powerful tool for elucidating the mechanisms of disease spread and guiding public health interventions. Such models can capture the progression of diphtheria outbreaks and predict their potential impact. Among them, the Susceptible-Latent-Infected-Recovered (SLIR) framework serves as a foundational model for studying diphtheria transmission dynamics and evaluating control strategies, including vaccination programs [1].

Research on the SLIR type model has employed a variety of numerical methods to better understand the dynamics of disease transmission. Traditionally, most studies have utilized fourth- and fifth-order Runge-Kutta or Euler methods to solve the classical SIR model. In recent years, the concept of fractional derivatives, real or complex derivatives of arbitrary order, has gained prominence in applied mathematics and mathematical analysis. Fractional differential equations have found extensive applications in modeling physical and biological systems [9]. By generalizing the concepts of integer-order differentiation and integration, fractional derivatives enable the simulation of multi-scale phenomena over broader time or length scales. Their non-local, power-law characteristics make fractional derivatives powerful tools for capturing memory and hereditary properties inherent in many physical processes, thus providing a more comprehensive framework for explaining complex biological dynamics.

The impact of infectious diseases such as diphtheria on population dynamics can be explored us-

ing fractional calculus, which offers a powerful framework for modeling complex epidemic processes. Fractional-order models provide greater flexibility in capturing memory effects and non-local interactions in disease transmission. While fractional derivatives have been successfully applied to study the dynamics of diseases such as dengue and HIV using real epidemiological data [20], research on fractional-order SLIR models for diphtheria has been done in Bangladesh. This gap highlights the potential for applying fractional modeling techniques to improve the understanding and prediction of diphtheria outbreaks, particularly in high-risk settings such as refugee camps and conflict-affected regions [17].

It is important to note that conventional mathematical models using integer-order derivatives, as well as standard nonlinear models, often fail to adequately capture the complexity observed in many real-world scenarios [19]. Since fractional derivatives offer a more accurate representation of such dynamics, this study employs a fractional-order SLIR model, based on the work of Md. Kamrujjaman et al., [3] to simulate diphtheria outbreaks in the Rohingya camps of Bangladesh. In this framework, the Caputo definition of the fractional derivative is utilized. First introduced by Michele Caputo in 1967, the Caputo fractional derivative is widely regarded as one of the most practical operators for real-world applications, as it naturally accommodates initial and boundary conditions [11]. Caputo fractional derivatives have been extensively applied to various epidemic models, including the SLIR model [2, 4, 25].

The Adams-Bashforth-Moulton Method (ABMM) is employed to obtain approximate solutions to the fractional differential equations. This method, originally developed by John Couch Adams, combines the Adams-Bashforth and Adams-Moulton schemes. In this predictor-corrector framework, the Adams-Bashforth method (ABM) serves as the predictor, while the Adams-Moulton method (AMM) functions as the corrector. Together, they form a multistep process that efficiently approximates solutions to differential equations [6]. One of the main advantages of fractional derivatives lies in their adaptability and non-local properties. Because these derivatives are of fractional order, they offer greater flexibility in modeling complex dynamics compared to classical derivatives [7]. Therefore, this study focuses on solving fractional-order derivatives using the ABM to simulate the diphtheria outbreak in the Rohingya camp in Bangladesh. Applying this method to fractional-order epidemiological models could enhance predictive accuracy and improve the design of intervention strategies, especially in high-risk populations and resource-limited settings. The proposed model provides a framework for evaluating the effects of vaccination and other control measures on diphtheria transmission. These insights can aid public health planning and outbreak response.

Objectives

- Develop a fractional-order SLIR model (in the Caputo sense) to simulate the transmission dynamics of diphtheria in Bangladesh.
- Numerically solve the fractional model using the Adams-Bashforth-Moulton predictor-corrector method for accuracy and stability.
- Validate the numerical performance of the fractional model through comparison with results obtained from the classical Runge-Kutta method.
- Analyze the impact of varying fractional orders (α) on the SLIR dynamics using graphical simulations to illustrate changes in disease progression.

The remainder of this paper is structured as follows. Section 2 presents the formulation of the fractional SLIR model for diphtheria transmission, including the definition of model compartments, governing equations, and the proof of non-negativity and boundedness of solutions. This section also describes the applied numerical methods, with particular emphasis on the Adams-Bashforth-Moulton predictor-corrector scheme for solving the fractional system. Section 3 reports the numerical results, comprising model validation, parameter estimation based on epidemiological data, and simulation outcomes under various fractional orders, accompanied by appropriate graphical illustrations. Section 4 concludes the paper with a summary of key findings, discusses the implications for outbreak control strategies, and outlines potential directions for future research.

2 Materials and Methods

2.1 SLIR formulation

In this paper, we propose an SLIR epidemic model to investigate the dynamics of diphtheria transmission within the Rohingya settlement [16, 18], as follows:

$$\begin{cases} \frac{dS}{dt} = \Lambda - \frac{\beta S(t)I(t)}{N} - \mu S(t), \\ \frac{dL}{dt} = l \frac{\beta S(t)I(t)}{N} - (\mu + \delta)L(t), \\ \frac{dI}{dt} = (1-l) \frac{\beta S(t)I(t)}{N} + \delta L(t) - (\mu + \gamma + \zeta)I(t), \\ \frac{dR}{dt} = \gamma I(t) - \mu R(t), \end{cases} \quad (1)$$

for $t \in (0, \infty)$, with the non-negative initial conditions:

$$S(0) = S_0, \quad L(0) = L_0, \quad I(0) = I_0, \quad \text{and} \quad R(0) = R_0. \quad (2)$$

Vaccination effects and waning immunity are not explicitly included in the present model. Although diphtheria vaccination plays a critical role in transmission dynamics, the available outbreak data do not provide time-resolved information on vaccination coverage, campaign timing, or immunity duration required to reliably identify additional parameters. To avoid over-parameterization, we focus on the baseline SLIR structure and capture delayed epidemic effects through the fractional-order formulation. The units of each parameter and epidemiological meaning are displayed in Table 1.

Table 1: Model parameters, epidemiological interpretation, and units

Parameter	Description	Units
Λ	Recruitment rate into the susceptible population	individuals/day
β	Transmission rate between susceptible and infectious individuals	day ⁻¹
δ	Progression rate from latent to infectious class	day ⁻¹
γ	Recovery rate of infectious individuals	day ⁻¹
μ	Natural mortality rate	day ⁻¹
ζ	Disease-induced mortality rate	day ⁻¹
l	Fraction of newly infected individuals entering the latent class	–
α	Fractional derivative order	–

All rate parameters are expressed in units of day^{-1} , while dimensionless parameters represent proportions or fractional orders.

Figure 1 illustrates the flow of individuals among the compartments defined in model (1).

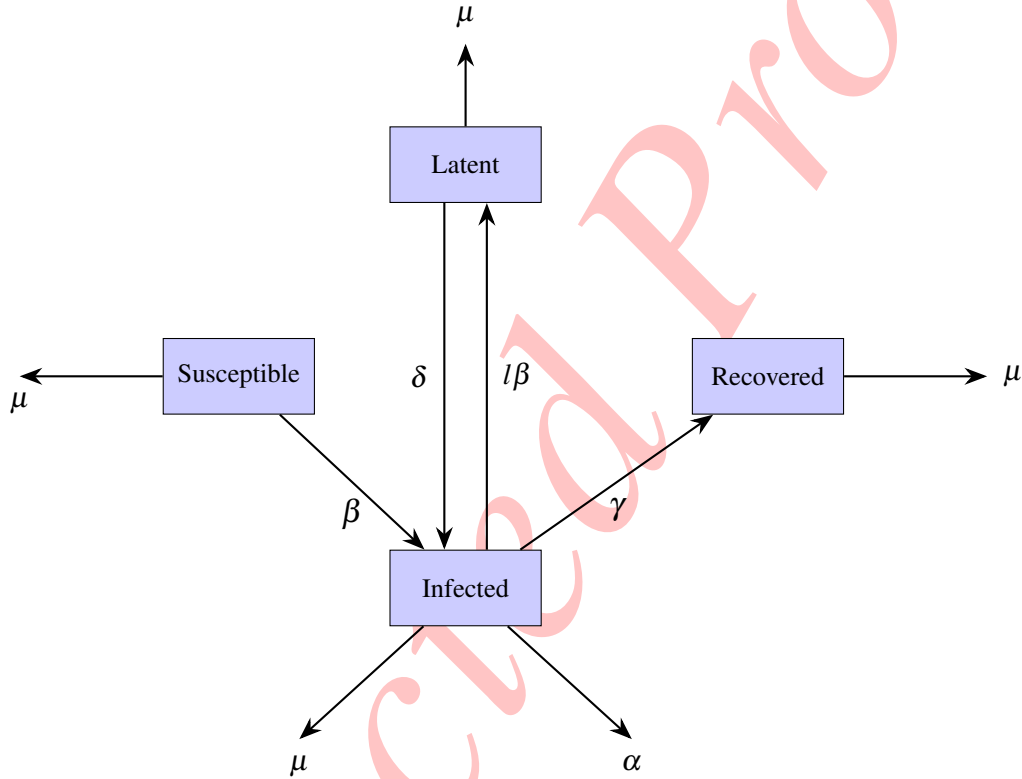


Figure 1: Schematic diagram of transmission dynamics of the SLIR model

The parameter Λ is the recruitment rate of the susceptible class, it is defined as $\frac{S_0}{\mu}$, where μ is the natural mortality rate. Moreover, ζ signifies the disease-induced death rate. The infection transmission rate is denoted by β . The δ stands for the detection rate of the latent population, and l restricts the infection for the L class. Following this, the detection rate δ regulates the transition from the L class to the I class. Assume N is fixed for a long time t , then

$$N(t) = S(t) + L(t) + I(t) + R(t). \quad (3)$$

Here, $N(t)$ is the total number of individuals subdivided into four compartments S, L, I and R which represent the number of populations in the susceptible, latent, infected and recovered class, respectively.

The SLIR model Eq. (1) can be expressed in dimensionless form by introducing the variables

$$S^* = \frac{S}{N}, \quad L^* = \frac{L}{N}, \quad I^* = \frac{I}{N}, \quad R^* = \frac{R}{N},$$

where N is the total population size.

Remark 1. *In refugee camp settings, the total population may vary due to migration, relocation, or administrative movements. In this study, the total population is assumed to remain effectively constant over the relatively short outbreak window used for model calibration. This approximation is commonly adopted in outbreak modeling when reliable time-dependent migration data are unavailable and allows tractable parameter estimation from reported case data. Nevertheless, unmodeled population inflows or outflows could influence transmission intensity and parameter estimates. Incorporating time-varying population dynamics through recruitment and migration terms is an important extension of the present framework and is left for future investigation.*

Hence, the dimensionless form of the SLIR model is given by

$$\begin{cases} \frac{dS^*}{dt} = \Lambda - \beta S^*(t)I^*(t) - \mu S^*(t), \\ \frac{dL^*}{dt} = l\beta S^*(t)I^*(t) - (\mu + \delta)L^*(t), \\ \frac{dI^*}{dt} = (1-l)\beta S^*(t)I^*(t) + \delta L^*(t) - (\mu + \gamma + \zeta)I^*(t), \\ \frac{dR^*}{dt} = \gamma I^*(t) - \mu R^*(t), \end{cases} \quad (4)$$

where S^* , L^* , I^* , and R^* denote the dimensionless proportions of susceptible, latent, infectious, and fully recovered individuals, respectively.

2.1.1 Applying fractional Caputo

The general initial value problem for the first-order differential equation is written as

$$\begin{aligned} Dy(x) &= f(x, y(x)), \\ y(0) &= y_0. \end{aligned} \quad (5)$$

The ordinary derivative model Eq. (1) is thus replaced by a fractional derivative in the following form

$$D_*^\alpha y(x) = f(x, y(x)), \quad (6)$$

where $\alpha > 0$ (but not necessarily $\alpha \in \mathbf{N}$). We will find a solution to this equation on the interval $[0, T]$, where T is an appropriate positive number. D_*^α is called Caputo type fractional derivative of order α .

Thus combining our fractional differential equation (6) with initial conditions, we have

$$y^k(0) = y_0^k, \quad k = 0, 1, \dots, m-1. \quad (7)$$

Let y be a function up to $(m-1)$ -order derivatives. Then the fractional Caputo derivative of order α is defined as

$$D_*^\alpha(y(x)) = \frac{1}{\Gamma(m-\alpha)} \int_0^x (x-t)^{m-\alpha-1} y^m(\Gamma(y)) dt, \quad (8)$$

where y^m denotes the m -th order integer derivative of y and Γ represents Gamma function, i.e., $\Gamma(y) = \int_0^\infty \xi^{y-1} e^{-\xi} d\xi$, where $y \in \mathbf{C}$. Therefore, the model is now described by a new system of fractional

differential equations (FDEs) as follows:

$$\begin{cases} D_t^\alpha S(t) = \Lambda - \beta S^*(t)I^*(t) - \mu S^*(t), \\ D_t^\alpha L(t) = l\beta S^*(t)I^*(t) - (\mu + \delta)L^*(t), \\ D_t^\alpha I(t) = (1-l)\beta S^*(t)I^*(t) + \delta L^*(t) - (\mu + \gamma + \zeta)I^*(t), \\ D_t^\alpha R(t) = \gamma I^*(t) - \mu R^*(t). \end{cases} \quad (9)$$

2.1.2 Solving fractional equation using ABMM

Fractional differential equations (FDEs) are generally challenging to solve analytically. Therefore, numerical methods must be employed. One of the most effective methods for solving fractional differential equations is the generalized ABMM. This method is a predictor-corrector technique specifically suited to handle the fractional Caputo derivative.

We discuss a numerical method for the fractional initial value problem

$$D_*^\alpha y(x) = f(x, y(x)), \quad y^k(0) = y_0^{(k)}, \quad k = 0, 1, \dots, [\alpha] - 1, \quad (10)$$

where the $y_0^{(k)}$ may be the arbitrary real numbers and $\alpha > 0$. In (10), $D_*^\alpha y(x) = f(x, y(x))$ denotes the differential operator in the sense of Caputo [10], defined by

$$D_*^\alpha y(x) = f(x, y(x)) = J^{n-\alpha} D^n z(t).$$

It is well known that the initial value problem (10) is equivalent to the Volterra integral equation

$$y(t) = \sum_{v=0}^{[\alpha]-1} y_0^{(v)} \frac{t^v}{v!} + \frac{1}{\Gamma(\alpha)} \int_0^t (t-u)^{\alpha-1} f(u, y(u)) du, \quad (11)$$

in the sense that a continuous function is a solution of (10) if and only if it is a solution of (11), (see [8]).

To illustrate our approach, we concentrate on the well-known initial-value problem for a first-order differential equation (5). We assume that the function f is such that a unique solution exists over some interval $[0, T]$. Then we consider a uniform grid $\{t_j = hj, j = 0, 1, \dots, N\}$ for the fractional Adam method with some integer N , $y = y(t_k)$, and step size $h = \frac{T}{N}$.

To derive the desired formula, we apply the product trapezoidal quadrature formula, using the weight function $(t_{k+1} - \cdot)^{\alpha-1}$ to approximate the integral, where nodes, $t_j, j = 0, 1, \dots, k+1$ as before. In other words, we employ the approximation technique,

$$\int_0^{t_{k+1}} (t_{k+1} - z)^{\alpha-1} g(z) dz \approx \int_0^{t_{k+1}} (t_{k+1} - z)^{\alpha-1} \tilde{g}_{k+1}(z) dz, \quad (12)$$

where, \tilde{g}_{k+1} represents the piecewise linear interpolant for g , with the nodes and knots selected at $t_j, j = 0, 1, \dots, k+1$. Using standard methods from quadrature theory (see [5]), the integral on the right-hand side of equation (12) can be written as:

$$\int_0^{t_{k+1}} (t_{k+1} - z)^{\alpha-1} \tilde{g}_{k+1}(z) dz = \sum_{j=0}^{k+1} a_{j,k+1} g(t_j), \quad (13)$$

where

$$a_{j,k+1} = \frac{h^\alpha}{\alpha(\alpha+1)} \begin{cases} (k^{\alpha+1} - (k-\alpha)(k+1)^\alpha), & \text{if } j=0, \\ (k-j+2)^{\alpha+1} + (k-j)^{\alpha+1} - 2(k-j+1)^{\alpha+1}, & \text{if } 1 \leq j \leq k, \\ 1, & \text{if } j=k+1. \end{cases} \quad (14)$$

This leads to our corrector formula, specifically the fractional version of the one-step AMM, which is given by:

$$y_{k+1} = \sum_{j=0}^{[\alpha]-1} y_0^{(j)} \frac{t_{k+1}^j}{j!} + \frac{1}{\Gamma(\alpha)} \left(\sum_{j=0}^k a_{j,k+1} f(t_j, y_j) + a_{k+1,k+1} f(t_{k+1}, y_{k+1}^P) \right). \quad (15)$$

To generalize the one-step ABM, we adopt a similar approach to that used in the Adams–Moulton technique; the integral on the right-hand side of equation (13) is replaced by the product rectangle rule

$$\int_0^{t_{k+1}} (t_{k+1} - z)^{\alpha-1} g(z) dz \approx \sum_{j=0}^k b_{j,k+1} g(t_j), \quad (16)$$

where

$$b_{j,k+1} = \frac{h^\alpha}{\alpha} ((k+1-j)^\alpha - (k-j)^\alpha). \quad (17)$$

Therefore, the predictor y_{k+1}^P is obtained using the Fractional ABM (FABM):

$$y_{k+1}^P = \sum_{j=0}^{[\alpha]-1} y_0^{(j)} \frac{t_{k+1}^j}{j!} + \frac{1}{\Gamma(\alpha)} \sum_{j=0}^k b_{j,k+1} f(t_j, y_j), \quad (18)$$

where the weights $\alpha_{j,k+1}$ and $b_{j,k+1}$ are established following the definitions provided in equations (14) and (18), respectively.

2.1.3 Numerical analysis

By using FABMM, the numerical solutions of the system of fractional differential equations (9) are formulated as follows:

$$\begin{cases} D^\alpha S(t) = f(t, S(t)), & S(0) = S_0, & 0 < \alpha < 1, t > 0 \\ D^\alpha L(t) = f(t, L(t)), & L(0) = L_0, \\ D^\alpha I(t) = f(t, I(t)), & I(0) = I_0, \\ D^\alpha R(t) = f(t, R(t)), & R(0) = R_0. \end{cases} \quad (19)$$

Substituting the SLIR right-hand sides f_S, f_L, f_I, f_R into the FABM predictor formula (18) and using the product-rectangle weights $b_{j,n+1}$ from (17) yields the component-wise predictor at t_{n+1} for the dimen-

sionless compartments, namely:

$$\begin{aligned}
 S_{n+1}^p &= S_0 + \frac{1}{\Gamma(\alpha)} \sum_{j=0}^n b_{j,n+1} (\Lambda - \beta S_j^* I_j^* - \mu S_j^*), \\
 L_{n+1}^p &= L_0 + \frac{1}{\Gamma(\alpha)} \sum_{j=0}^n b_{j,n+1} (l \beta S_j^* I_j^* - (\mu + \delta) L_j^*), \\
 I_{n+1}^p &= I_0 + \frac{1}{\Gamma(\alpha)} \sum_{j=0}^n b_{j,n+1} ((1-l) \beta S_j^* I_j^* + \delta L_j^* - (\mu + \gamma + \zeta) I_j^*), \\
 R_{n+1}^p &= R_0 + \frac{1}{\Gamma(\alpha)} \sum_{j=0}^n b_{j,n+1} (\gamma I_j^* - \mu R_j^*),
 \end{aligned} \tag{20}$$

where

$$b_{j,k+1} = \frac{h^\alpha}{\alpha} ((k+1-j)^\alpha - (k-j)^\alpha), \tag{21}$$

$$\begin{aligned}
 S_{n+1}^* &= S_0^* + \frac{h^\alpha}{\Gamma(\alpha+2)} \left[f_S(t_{n+1}, S_{n+1}^{*p}, L_{n+1}^{*p}, I_{n+1}^{*p}, R_{n+1}^{*p}) + \sum_{j=0}^n a_{j,n+1} f_S(t_j, S_j^*, L_j^*, I_j^*, R_j^*) \right], \\
 L_{n+1}^* &= L_0^* + \frac{h^\alpha}{\Gamma(\alpha+2)} \left[f_L(t_{n+1}, S_{n+1}^{*p}, L_{n+1}^{*p}, I_{n+1}^{*p}, R_{n+1}^{*p}) + \sum_{j=0}^n a_{j,n+1} f_L(t_j, S_j^*, L_j^*, I_j^*, R_j^*) \right], \\
 I_{n+1}^* &= I_0^* + \frac{h^\alpha}{\Gamma(\alpha+2)} \left[f_I(t_{n+1}, S_{n+1}^{*p}, L_{n+1}^{*p}, I_{n+1}^{*p}, R_{n+1}^{*p}) + \sum_{j=0}^n a_{j,n+1} f_I(t_j, S_j^*, L_j^*, I_j^*, R_j^*) \right], \\
 R_{n+1}^* &= R_0^* + \frac{h^\alpha}{\Gamma(\alpha+2)} \left[f_R(t_{n+1}, S_{n+1}^{*p}, L_{n+1}^{*p}, I_{n+1}^{*p}, R_{n+1}^{*p}) + \sum_{j=0}^n a_{j,n+1} f_R(t_j, S_j^*, L_j^*, I_j^*, R_j^*) \right],
 \end{aligned} \tag{22}$$

and

$$a_{j,n+1} = \frac{h^\alpha}{\alpha(\alpha+1)} \begin{cases} (n^{\alpha+1} - (n-\alpha)(n+1)^\alpha), & \text{if } j = 0, \\ ((n-j+2)^{\alpha+1} + (n-j)^{\alpha+1} - 2(n-j+1)^{\alpha+1}), & \text{if } 1 \leq j \leq n, \\ 1, & \text{if } j = n+1. \end{cases} \tag{23}$$

The results obtained from simulations using the above equations will be discussed in the following section. For clarity, all notation is used consistently throughout the manuscript and summarized where appropriate.

2.1.4 Data and preprocessing

The epidemiological data used in this study were obtained from publicly available outbreak reports documenting the diphtheria epidemic among Rohingya refugees in Cox's Bazar, Bangladesh, during the period 2017-2019 [21, 24]. The dataset consists of reported daily case counts collected through field surveillance during the early outbreak phase. Due to limited laboratory confirmation capacity in humanitarian and emergency settings, the reported data include suspected and clinically diagnosed cases

Table 2: Reported cumulative diphtheria cases in Cox’s Bazar, Bangladesh, based on WHO epidemiological bulletin (November–December 2017)

Days index			Days index		
Day	Date	Cumulative cases	Day	Date	Cumulative cases
1	10 Nov 2017	1	16	25 Nov 2017	605
2	11 Nov 2017	2	17	26 Nov 2017	746
3	12 Nov 2017	3	18	27 Nov 2017	859
4	13 Nov 2017	4	19	28 Nov 2017	1027
5	14 Nov 2017	7	20	29 Nov 2017	1190
6	15 Nov 2017	9	21	30 Nov 2017	1334
7	16 Nov 2017	13	22	01 Dec 2017	1479
8	17 Nov 2017	24	23	02 Dec 2017	1607
9	18 Nov 2017	45	24	03 Dec 2017	1732
10	19 Nov 2017	59	25	04 Dec 2017	1846
11	20 Nov 2017	75	26	05 Dec 2017	1944
12	21 Nov 2017	117	27	06 Dec 2017	2070
13	22 Nov 2017	206	28	07 Dec 2017	2140
14	23 Nov 2017	277	29	08 Dec 2017	2248
15	24 Nov 2017	460	30	09 Dec 2017	2358
			31	10 Dec 2017	2438

in addition to laboratory-confirmed cases, consistent with outbreak surveillance practices at the time. For parameter estimation, the calibration window was restricted to the first 50 days of reported cases, corresponding to the period of sustained transmission with relatively consistent reporting intensity. To reduce reporting noise, daily case counts were aggregated to cumulative case totals for model fitting. Missing or delayed reports were not explicitly corrected due to the absence of detailed reporting metadata; therefore, the observations are treated as reported case counts. As a result, the estimated parameters should be interpreted as effective parameters reflecting both the underlying transmission dynamics and the reporting process. Table 2 shows corresponding to the WHO epidemiological bulletin (Distribution in time of presentation of cases). Day 1 corresponds to 10 November 2017, and subsequent days represent consecutive reporting dates from the WHO epidemiological bulletin.

2.1.5 Parameter estimation procedure

Let $C_{obs}(t_i)$ denote the observed cumulative number of diphtheria cases at time t_i , and let $C_{mod}(t_i; \theta)$ denote the corresponding model-generated cumulative cases obtained from the SLIR system with parameter vector θ . We compute the model-predicted cumulative cases as $C_{mod}(t_i; \theta) = N_0(L^*(t_i) + I^*(t_i) + R^*(t_i))$, so that C_{mod} counts everyone ever infected (latent, infectious, or recovered). Model parameters were estimated by minimizing the nonlinear least-squares objective function

$$J(\theta) = \sum_{i=1}^n [C_{obs}(t_i) - C_{mod}(t_i; \theta)]^2.$$

The minimization was carried out using MATLAB’s GlobalSearch algorithm combined with Latin hypercube sampling to reduce sensitivity to initial guesses and local minima. The model was calibrated over

Table 3: Parameter bounds used in the GlobalSearch and Latin hypercube sampling procedure

Parameter	Description	Lower bound	Upper bound	Units
β	Transmission rate	10^{-8}	10^{-2}	day ⁻¹
γ	Recovery rate	0.01	2	day ⁻¹
δ	Latent detection rate	10^{-3}	1	day ⁻¹
μ	Natural mortality rate	10^{-5}	10^{-2}	day ⁻¹
ζ	Disease-induced death rate	10^{-8}	10^{-2}	day ⁻¹
l	Fraction entering latency	0	1	–
Λ	Recruitment rate	0	500	individuals/day

the first 50 days of reported cases. Parameter bounds were selected based on epidemiological plausibility and previously reported values in the literature and are summarized in Table 3.

2.2 Threshold analysis and well-posedness

2.2.1 Disease-free equilibrium and basic reproduction number R_0

Consider the fractional SLIR model ($0 < \alpha \leq 1$):

$$\begin{aligned}
 D_t^\alpha S &= \Lambda - \beta \frac{SI}{N} - \mu S, \\
 D_t^\alpha L &= l \beta \frac{SI}{N} - (\mu + \delta)L, \\
 D_t^\alpha I &= (1-l) \beta \frac{SI}{N} + \delta L - (\mu + \gamma + \zeta)I, \\
 D_t^\alpha R &= \gamma I - \mu R,
 \end{aligned} \tag{24}$$

with $N(t) = S + L + I + R$. The disease-free equilibrium (DFE) is

$$E_0 = (S^*, L^*, I^*, R^*) = \left(\frac{\Lambda}{\mu}, 0, 0, 0 \right).$$

Following the next-generation approach, take the infected-state vector $x = (L, I)^\top$. At the DFE we have $S^*/N^* = 1$. The *new-infection* terms $\mathcal{F}(x)$ and the *transition* terms $\mathcal{V}(x)$ can be written (linearized at E_0) as

$$\mathcal{F} = \begin{pmatrix} l\beta I \\ (1-l)\beta I \end{pmatrix}, \quad \mathcal{V} = \begin{pmatrix} (\delta + \mu)L \\ -(\delta)L + (\gamma + \zeta + \mu)I \end{pmatrix}.$$

Hence

$$F = \begin{pmatrix} 0 & l\beta \\ 0 & (1-l)\beta \end{pmatrix}, \quad V = \begin{pmatrix} \delta + \mu & 0 \\ -\delta & \gamma + \zeta + \mu \end{pmatrix}, \quad V^{-1} = \begin{pmatrix} \frac{1}{\delta + \mu} & 0 \\ \frac{\delta}{(\delta + \mu)(\gamma + \zeta + \mu)} & \frac{1}{\gamma + \zeta + \mu} \end{pmatrix}.$$

The next-generation matrix is $K = FV^{-1}$. Since F has rank 1, K is rank 1 and its unique nonzero eigenvalue equals $R_0 = \rho(K) = v^\top u$ for the factorization $K = uv^\top$, where

$$u = \begin{pmatrix} l\beta \\ (1-l)\beta \end{pmatrix}, \quad v^\top = \begin{pmatrix} \delta \\ (\delta + \mu)(\gamma + \zeta + \mu), \frac{1}{\gamma + \zeta + \mu} \end{pmatrix}.$$

Therefore

$$R_0 = \beta \left[\frac{l\delta}{(\delta + \mu)(\gamma + \zeta + \mu)} + \frac{1-l}{\gamma + \zeta + \mu} \right]. \quad (25)$$

Remarks. (i) If all new infections pass through latency ($l = 1$), (25) reduces to $R_0 = \frac{\beta\delta}{(\delta + \mu)(\gamma + \zeta + \mu)}$.

(ii) If all new infections go directly to I ($l = 0$), then $R_0 = \frac{\beta}{\gamma + \zeta + \mu}$.

Local stability of the DFE. In the integer-order limit $\alpha = 1$, the DFE is locally asymptotically stable if $R_0 < 1$ and unstable if $R_0 > 1$. For $0 < \alpha < 1$, the linearized fractional system inherits the same threshold condition with Mittag–Leffler-type decay.

2.2.2 Positivity and invariant region

Lemma 1 (Positivity). *Let the initial data satisfy $S(0), L(0), I(0), R(0) \geq 0$ and parameters be nonnegative. Then the solution of (24) satisfies $S(t), L(t), I(t), R(t) \geq 0$ for all $t \geq 0$.*

Proof. We write (24) in Volterra form using the Caputo integral representation (for $0 < \alpha < 1$):

$$y(t) = y(0) + \frac{1}{\Gamma(\alpha)} \int_0^t (t - \tau)^{\alpha-1} f(\tau, y(\tau)) d\tau,$$

componentwise for $y \in \{S, L, I, R\}$. The kernels $(t - \tau)^{\alpha-1}/\Gamma(\alpha)$ are nonnegative, and each right-hand side f is of the form “inflows – nonnegative multiples of the state”, so the integrals preserve nonnegativity provided the initial data are nonnegative. A standard contradiction argument (using first exit from $\mathbb{R}^4 \geq 0$). \square

Theorem 1 (Invariant region and boundedness). *Let $\Omega = \{(S, L, I, R) \in \mathbb{R}^4 \geq 0 : S + L + I + R \leq \Lambda/\mu\}$. Then every solution with nonnegative initial data enters Ω in finite time and remains there.*

Proof. Summing (24) gives

$$D_t^\alpha N(t) = \Lambda - \mu N(t) - \zeta I(t) \leq \Lambda - \mu N(t).$$

By comparison with the scalar fractional equation $D_t^\alpha z(t) = \Lambda - \mu z(t)$ (with explicit solution in terms of the Mittag–Leffler function), we have $N(t) \leq \max\{N(0), \Lambda/\mu\}$ for all $t \geq 0$. Together with Lemma 1, this implies forward invariance of Ω . \square

3 Results and discussion

This section presents the numerical results for the SLIR model described in Eq. (20), focusing on the susceptible, latent, infectious, and recovered populations. Since model (1) represents a population system and tracks the dynamics of disease outbreaks among individuals, all dependent variables and parameters are required to be non-negative. To achieve an optimal fit to observed data, methods such as fitting to longitudinal daily case notification data, the least-squares approach, and Latin hypercube sampling are utilized. In the proposed model, key parameters, including ζ, β, γ, l and δ , re estimated using the least-squares method. The MATLAB GlobalSearch algorithm is employed in conjunction with Latin hypercube sampling to identify the most appropriate parameter values. The best-fit parameter estimates, based on the model and data, are $\zeta = 0.0000025, \beta = 0.000011625, \gamma = 0.8975, \Lambda = 60, \mu = 0.002, l = 0.005, \delta = 0.01$, and are subsequently used in the numerical simulations.

Outbreak data collected in humanitarian and refugee settings are subject to several limitations, including underreporting, reporting delays, evolving case definitions, and limited laboratory confirmation. In the present study, only a small proportion of reported cases were laboratory confirmed, and surveillance intensity may vary over time. As a result, the estimated parameters should be interpreted as effective parameters conditioned on the available reporting process rather than precise biological constants. These data limitations may influence parameter uncertainty and forward projections. Future studies could incorporate reporting-rate models or formal uncertainty quantification methods, such as bootstrap or Bayesian approaches, when richer surveillance data become available.

Model 1 is a system of first-order Ordinary Differential Equations (ODEs) with initial conditions. Traditionally, well-known numerical schemes such as the Euler method, AMM, Backward Differentiation Formula (BDF), linear multistep methods, Runge-Kutta methods, and Finite Difference Methods (FDM) [24,25] are applied to solve such systems. In this study, instead of using the classical fourth-order Runge-Kutta method, which is effective for integer-order systems, we adopt the fractional Adams-Bashforth-Moulton predictor-corrector scheme. This method is particularly suited for fractional-order differential equations due to its higher-order accuracy, stability properties, and ability to handle the memory effect inherent in fractional derivatives, making it an ideal choice for simulating the fractional SLIR model.

3.1 Parameter uncertainty and sensitivity analysis

Uncertainty in parameter estimates arises primarily from reporting variability, limited laboratory confirmation, and potential delays in case notification inherent to outbreak data collected in humanitarian settings. To assess the robustness of the calibrated model, a local sensitivity analysis was performed by perturbing each estimated parameter by $\pm 10\%$ around its fitted value while holding all other parameters fixed.

The resulting changes in key epidemiological outputs, including peak infection size and time to peak, indicate that the transmission rate β and recovery rate γ exert the strongest influence on epidemic dynamics. Moderate variations in the latent detection rate δ and disease-induced mortality rate ζ produce comparatively smaller changes, while the fractional order α primarily affects the timing and duration of epidemic waves rather than peak magnitude.

Due to the absence of detailed individual-level data and time-resolved vaccination or reporting-rate information, formal confidence intervals or posterior distributions were not estimated in this study. Con-

sequently, the reported parameter values should be interpreted as effective estimates that capture dominant outbreak behavior under the available surveillance process. Incorporating formal uncertainty quantification methods, such as bootstrap resampling or Bayesian inference, is an important direction for future work when richer epidemiological data become available. Local sensitivity analysis is summarized in Table 4.

Table 4: Summary of local sensitivity analysis based on $\pm 10\%$ parameter perturbations

Parameter	Effect on peak size	Effect on peak timing
β	High	Moderate
γ	High	Moderate
δ	Moderate	Low
ζ	Low	Low
α	Moderate	High

3.2 Model-data comparison

To assess the ability of the proposed model to reproduce the observed outbreak dynamics, a quantitative model–data comparison was performed using officially reported epidemiological data. Observed cumulative diphtheria case counts were obtained from the World Health Organization epidemiological bulletin reporting the temporal distribution of cases in Cox’s Bazar, Bangladesh, during November–December 2017. Model-predicted cumulative cases were computed as the total number of individuals who had experienced infection up to time t , defined as

$$C_{\text{mod}}(t) = I(t) + R(t), \quad (26)$$

where $I(t)$ and $R(t)$ denote the infectious and recovered populations, respectively. To ensure consistency with the reported data, model variables were scaled to absolute population counts. Figure 2 presents the comparison between reported cumulative case counts and the model-generated epidemic trajectory over the observation period. The model captures the overall growth trend of the outbreak, including the rapid escalation phase followed by a gradual slowing of case accumulation. To quantify the agreement between observed and simulated dynamics, the root mean square error (RMSE) was computed as

$$\text{RMSE} = \sqrt{\frac{1}{n} \sum_{i=1}^n (C_{\text{obs}}(t_i) - C_{\text{mod}}(t_i))^2}, \quad (27)$$

where $C_{\text{obs}}(t_i)$ denotes the reported cumulative cases at time t_i and n is the number of observation points. Model parameters were calibrated by minimizing RMSE over the observation interval. The resulting RMSE value was found to be $\text{RMSE} = 363.661$. The obtained RMSE is small relative to the epidemic magnitude, indicating a satisfactory agreement between reported data and model predictions. Remaining discrepancies between observed and simulated trajectories may be attributed to reporting delays, heterogeneous contact patterns, and the simplifying assumptions of homogeneous mixing inherent in the model formulation.

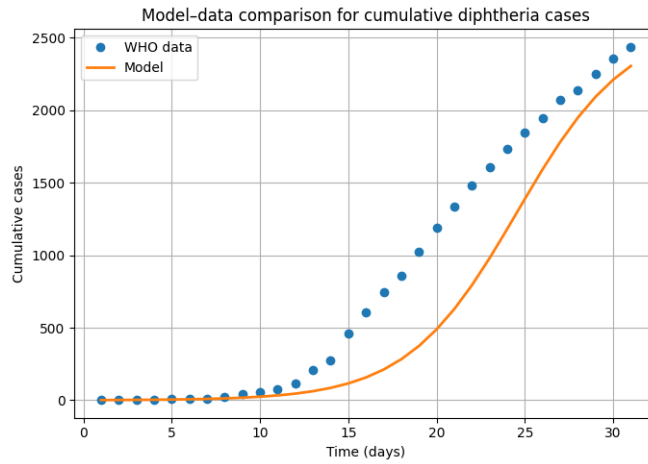


Figure 2: Comparison between reported WHO cumulative diphtheria cases and the model-generated epidemic trajectory

3.3 Validation of the study

To verify the numerical implementation, we first consider the limiting case $\alpha = 1$, for which the fractional SLIR system reduces to a classical first-order ODE model. In this setting, we benchmark the fractional ABM predictor-corrector scheme against MATLAB[®] built-in fourth-order Runge-Kutta (RK4) solver. Both methods are run on the same time grid with identical step size, parameters, and initial conditions, and the trajectories of all compartments $S(t), L(t), I(t), R(t)$ are recorded at the reporting times t (days) shown in Table 5. The two solutions coincide to the displayed precision, with any discrepancy confined to the last reported digit. This confirms that the ABM code correctly reproduces the classical dynamics when $\alpha = 1$ and introduces no spurious numerical artifacts. For genuinely fractional orders $\alpha \in (0, 1)$, closed-form reference solutions are unavailable. We therefore assess numerical consistency by mesh refinement: the ABM scheme is run with step sizes $h, h/2$, and $h/4$, and the differences between successive grids are monitored for each compartment. The errors decrease monotonically under step halving, indicating convergence of the scheme across all state variables. In addition, qualitative invariants are preserved throughout: numerical solutions remain non-negative, and the total population evolves in accordance with the modeled recruitment and removal terms, thereby verifying biological feasibility of the computations.

3.4 Mesh refinement and observed convergence

To examine numerical reliability, a mesh-refinement study was performed by repeating the simulation with successively smaller time steps $h, h/2$, and $h/4$ over the same time horizon. Let $I_h(t)$ denote the numerical approximation of the infected component obtained with step size h . Following standard practice, the refinement error was estimated using the difference between two successive discretizations,

$$E(h) = \|I_h - I_{h/2}\|_2$$

Table 5: Numerical results of solving SIR model with $\alpha = 1$

Time (days)	Population							
	Runge-Kutta				Adams Bashforth Moulton			
	$S(t)$	$L(t)$	$I(t)$	$R(t)$	$S(t)$	$L(t)$	$I(t)$	$R(t)$
0	0.994000	0.005000	0.001000	0.000000	0.994000	0.005000	0.001000	0.000000
5	0.984110	0.004709	0.000825	0.000406	0.984111	0.004709	0.000825	0.000406
10	0.974320	0.004435	0.000704	0.000743	0.974321	0.004435	0.000704	0.000743
15	0.964620	0.004176	0.000617	0.001030	0.964621	0.004176	0.000617	0.001030
20	0.955020	0.003933	0.000551	0.001280	0.955021	0.003933	0.000551	0.001281
25	0.945520	0.003704	0.000501	0.001503	0.945521	0.003704	0.000501	0.001503
30	0.936110	0.003488	0.000460	0.001703	0.936111	0.003488	0.000460	0.001703
35	0.926800	0.003285	0.000425	0.001884	0.926801	0.003285	0.000425	0.001884
40	0.917580	0.003094	0.000396	0.002049	0.917581	0.003094	0.000396	0.002049
45	0.908450	0.002914	0.000370	0.002200	0.908451	0.002914	0.000370	0.002201
50	0.899410	0.002744	0.000347	0.002338	0.899411	0.002744	0.000347	0.002338
55	0.890460	0.002584	0.000325	0.002467	0.890461	0.002584	0.000325	0.002468
60	0.881600	0.002434	0.000306	0.002582	0.881601	0.002434	0.000306	0.002582
65	0.872830	0.002292	0.000287	0.002689	0.872831	0.002292	0.000282	0.002695
70	0.864140	0.002159	0.000270	0.002788	0.864141	0.002159	0.000280	0.002778

computed on the common time grid. The observed convergence order was then estimated by

$$p \approx \log_2 \left(\frac{E(h)}{E(h/2)} \right).$$

The results in Table 6 show decreasing error under step refinement and an observed convergence behavior consistent with the expected stability and convergence properties of the fractional ABM scheme.

Table 6: Mesh-refinement study for the FABM method (illustrative error based on successive refinements)

Step size	$E(h) = \ I_h - I_{h/2}\ _2$	$E(h/2) = \ I_{h/2} - I_{h/4}\ _2$	Observed order p
h	$3.461393e^{-05}$	$1.705801e^{-05}$	1.0209

3.5 Epidemiological interpretation of the fractional order

In the Caputo fractional formulation, the order $\alpha \in (0, 1]$ controls the strength of memory effects in the system through a power-law kernel. Smaller values of α correspond to stronger history dependence, reflecting delayed responses, persistent transmission effects, or heterogeneity in contact and recovery processes, while $\alpha = 1$ recovers the classical memory-less model.

In the context of diphtheria transmission, such memory effects may represent delayed behavioral changes, prolonged infectiousness, or accumulated exposure in high-density camp environments. To identify epidemiologically reasonable values of α , multiple fractional orders were examined, and model

trajectories were compared with reported case data using the same fitting criterion. Values of α greater than 0.5 were found to provide the best balance between data fidelity and biological plausibility and were therefore adopted in the numerical simulations.

3.6 SLIR simulation

Since 25 August 2017, violence in Myanmar’s Rakhine State has pushed about 655,000 Rohingya into Cox’s Bazar, swelling an existing displaced population of roughly 300,000. Diphtheria cases now cluster mainly in Balukhali’s makeshift and extension camps, with spread to Kutupalong, Thangkhal, Jamtoli and Nayapara, where malnutrition, scant immunisation and inadequate water-sanitation services heighten disease risk. By 26 December 2017, field surveillance had recorded 2,526 suspected diphtheria infections among Rohingya refugees, with an abrupt surge of 96 new presentations to treatment centers on that single day and a cumulative 27 deaths, just over a 1% case-fatality ratio. The age profile reveals that school-aged children shoulder most of the burden: 14% of cases occur in children 0 – 5 years, 34% in those 5 – 10 years, and 27% in early adolescents 10 – 15 years, leaving only 25% of infections among individuals older than 15 years. Timeliness of care is a key determinant of outcome—patients typically seek help two days after symptom onset, yet fatalities have been linked to a median six-day delay, prompting health partners to scale up active case-finding, simplify referral pathways and intensify community awareness so that symptomatic individuals reach antitoxin and antibiotic therapy before complications ensue. The epidemic curve shown in Figure 3, from [24], complements these statistics by depicting a steep, sustained rise in incident cases through early to mid December, visually confirming ongoing transmission and underscoring the urgency of the strengthened interventions.

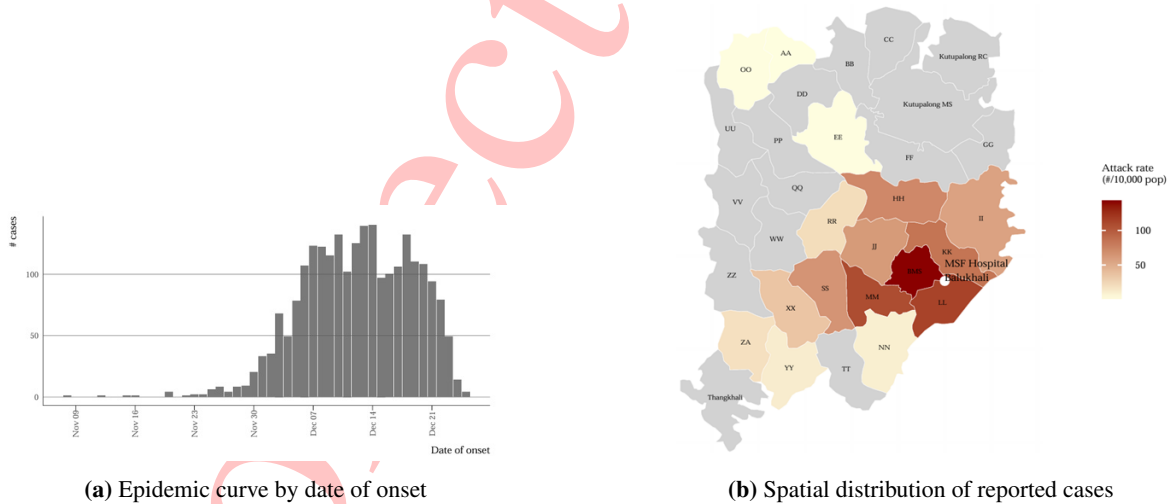


Figure 3: Epidemiological characteristics of the diphtheria outbreak: (a) epidemic curve by date of onset and (b) spatial distribution of reported cases in Cox’s Bazar, Bangladesh [24]

Building on this overview, Diphtheria is an acute and highly contagious respiratory disease caused by *Corynebacterium diphtheriae* and transmitted chiefly via respiratory droplets or close physical contact. Where, Panel (a) of Figure 4 bar charts the laboratory-confirmed daily case counts recorded in Balukhali Rohingya Camp during the first 50 days of the outbreak. Case numbers remained sporadic for roughly

the initial 20 days, but climbed rapidly thereafter, surpassing 50 per day by day 25 and reaching their apex between days 25 and 35, before beginning a gradual decline. In contrast, Panel (b) of Figure 4 depicts the corresponding cumulative case curve, which exceeds 2000 infections by day 50. This trajectory provides the empirical basis for the forward projections presented in subsequent figures.

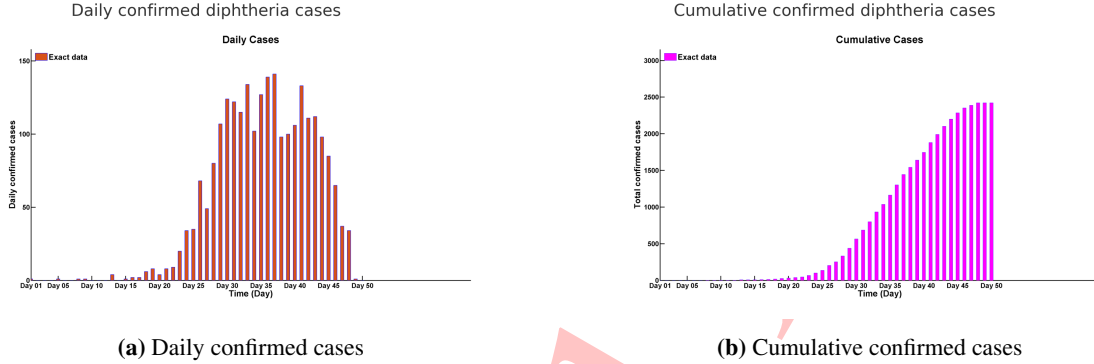


Figure 4: Bar charts illustrating (a) daily confirmed diphtheria cases and (b) cumulative case counts

These observed patterns underscore the rapid escalation and subsequent partial containment of the outbreak within a relatively short time frame. The initial sporadic cases likely reflect localized transmission before the disease gained momentum in the camp's dense population. The sharp rise between days 20 and 35 suggests a period of intense person-to-person spread, potentially linked to overcrowding and delayed intervention measures. The subsequent decline may be attributed to the implementation of case management strategies, isolation measures, and administration of Diphtheria Anti Toxin (DAT). These trends not only validate the urgency of timely public health interventions but also form a critical foundation for calibrating the SLIR model to simulate and forecast outbreak dynamics.

Figure 2 compares the observed cumulative diphtheria case counts with the model-generated cumulative trajectory obtained from the fractional-order SLIR system over the 50-day calibration window. The model captures the overall growth pattern and timing of the outbreak with good agreement, particularly during the rapid escalation phase. To quantitatively assess the goodness of fit, the root mean square error (RMSE) was computed between observed and simulated cumulative case counts according to

$$\text{RMSE} = \sqrt{\frac{1}{n} \sum_{i=1}^n (C_{\text{obs}}(t_i) - C_{\text{mod}}(t_i))^2}.$$

For the fitted model, the RMSE over the calibration period was found to be 363.661.

The dynamic behavior of the SLIR model is examined using simulation curves generated by the FABMM.

Figure 5 shows that the susceptible fraction $S^*(t)$ collapses more quickly as the fractional index α increases. When $\alpha = 0.50$, $S^*(t)$ does not reach zero until roughly day 63, increasing α to 0.60, 0.70, 0.80, and 0.90 shortens this interval to about 55, 46, 41, and 37 days, respectively. The downturn also begins earlier for larger α : all curves remain close to one during the first 15-20 days, yet the $\alpha = 0.90$ trajectory starts its sharp descent soon after day 20, almost ten days before the $\alpha = 0.50$. Thus, higher fractional orders, which embed less long-range memory, accelerate the depletion of susceptible

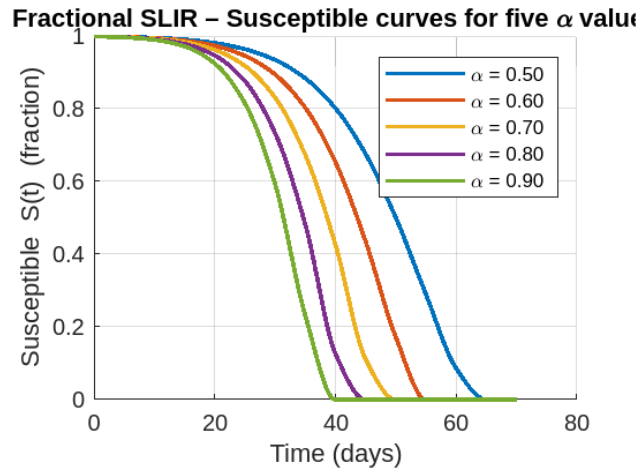


Figure 5: Time evolution of the susceptible population $S(t)$ under varying fractional orders α , highlighting the influence of memory effects on epidemic onset. Lower α values maintain higher susceptible levels for a longer duration, while higher α accelerates depletion

and foreshorten the epidemic wave. Figure 6 reveals that the latent fraction $L^*(t)$ remains a transient, low-amplitude compartment whose timing and magnitude are nonetheless sensitive to the fractional order α . Latents begin to accumulate around day 20 for every scenario, but higher α values provoke a steeper ascent and an earlier, slightly taller crest: $\alpha = 0.90$ peaks first, near day 34, reaching just over 6% of the population, followed in two-day increments by $\alpha = 0.80$ ($\approx 5\%$), 0.70 ($\approx 4\%$), 0.60 ($\approx 3\%$) and 0.50 ($\approx 2\%$). After each apex the curves decay almost linearly, converging toward zero by day 60, so the entire latent stage spans roughly 40 days for $\alpha = 0.90$ and extends to nearly 50 days for $\alpha = 0.50$. The ordering mirrors that observed in the infected and recovered compartments: larger α (weaker memory) accelerates progression into, and exit from, latency, producing a shorter yet more concentrated surge, whereas smaller α drags the latent tail forward, lowers the peak load, and lengthens the period during which individuals silently incubate infection. Figure 7 reveals that the infected fraction $I^*(t)$ climbs more steeply and peaks sooner as the fractional order α rises. For $\alpha = 0.90$ the outbreak accelerates rapidly, cresting near 0.95 of the population around day 44 before plunging back to zero within the next 15 days. Lowering the order elongates the wave: with $\alpha = 0.80$ the peak (≈ 0.83) arrives at day 46; $\alpha = 0.70$ reaches about 0.75 at day 50; $\alpha = 0.60$ tops out near 0.71 around day 54, and $\alpha = 0.50$ is still climbing past day 60, eventually plateauing just below 0.70. Thus, higher fractional orders—encoding weaker memory—produce sharper, higher surges that burn through susceptible quickly, whereas lower orders dampen the growth rate, delay the apex, and stretch the epidemic tail. Figure 8 demonstrates a strict, time-ordered acceleration in the cumulative-recovery fraction $R^*(t)$ as the fractional order α rises: after an almost quiescent first 20 days, the $\alpha = 0.90$ curve breaches 10% recovery by day 31 and passes the 80% milestone at day 46, followed in 5- to 7-day increments by $\alpha = 0.80$ (day 51), 0.70 (day 58), 0.60 (day 66) and finally 0.50 , which still lags below 80% at the simulation horizon. Over the explosive-growth window (\approx days 30-50) the maximum slope dR^*/dt for $\alpha = 0.90$ is more than twice that of $\alpha = 0.50$, underscoring how weaker memory kernels (higher α) compress the epidemic into a briefer, more intense episode, whereas stronger memory (lower α) stretches both the rise and the tail of the outbreak, delaying population-level convalescence by up to three weeks.

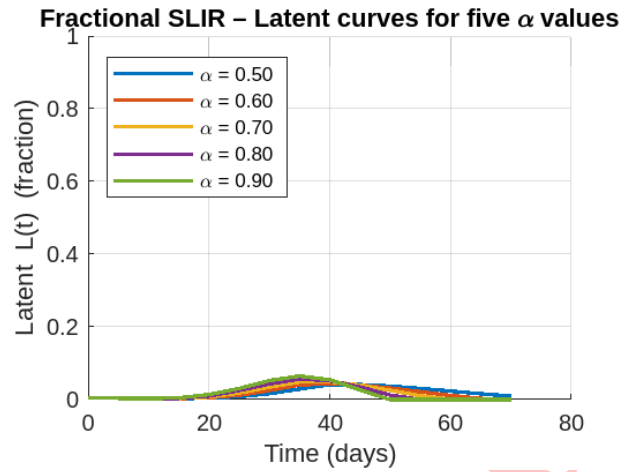


Figure 6: Time evolution of the latent population $L(t)$ for different fractional orders α in the SLIR framework. Reduced α values lead to delayed peak formation and prolonged latency, whereas larger α values shorten the latent phase

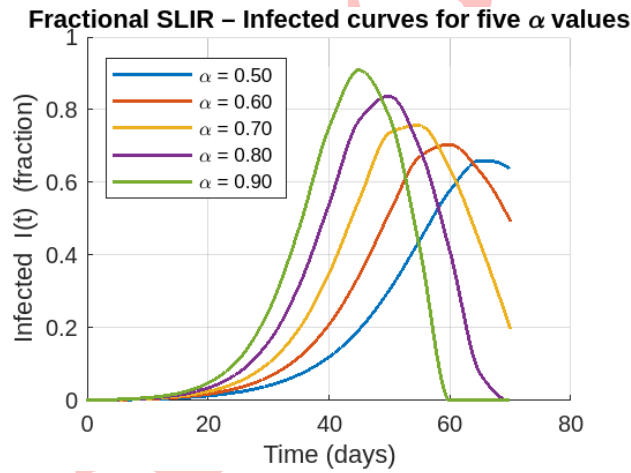


Figure 7: Dynamics of the infectious population $I(t)$ for various fractional orders α . Smaller α values reduce peak infection levels and delay outbreak peaks, while larger α values yield higher and earlier infection peaks

4 Conclusion

In conclusion, the simulated results showed that the FABMM can reliably solve the fractional SLIR model calibrated to the 2017 Rohingya diphtheria outbreak. The FABMM solver was 2-3 times faster for identical tolerance settings, largely because it avoids repeated Jacobian evaluations and exploits the intrinsic predictor-corrector reuse of function calls. All simulations and parameter estimation were performed in MATLAB (R2025b) on a standard desktop workstation. The fractional ABM method was stable for the investigated fractional orders and step sizes. Since extensive hardware-level benchmarking and profiling were beyond the scope of this study, we do not claim definitive computational superiority over alternative solvers. Reported numerical results should therefore be interpreted based on accuracy

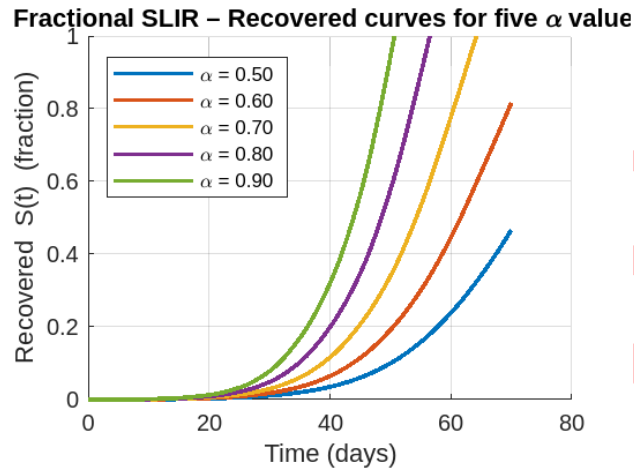


Figure 8: Recovery dynamics $R(t)$ in the SLIR model with different fractional orders α . Lower α values slow the accumulation of recovered individuals, whereas higher α values lead to faster convergence toward the disease-free state

and stability rather than wall-clock speed alone. The incorporation of fractional-order derivatives enhanced the model's ability to capture the memory effects inherent in epidemic progression, providing a more flexible and realistic description compared to classical integer-order approaches. This method is valid and robust, since the outcomes obtained at $\alpha = 1$ match the reference Runge-Kutta-4 solution, while fractional orders $0.5 \leq \alpha < 1$ recreate the observed transmission and recovery patterns in the Cox's Bazar Rohingya camps with markedly lower computational cost. Different sets of derivative order, α , were tested to identify the fractional exponent that most closely reproduces field data; values above 0.5 proved epidemiologically acceptable, shortening the time to peak infection and accelerating convergence to herd-level recovery. Moreover, the dynamics of the SLIR model across Figures 5-8 reveal the influence of varying fractional-order values (α) on disease progression. For lower α values, all compartments evolve more slowly, reflecting memory effects that delay the epidemic's peak and prolong the transient phases. In Figure 5, susceptible populations decline more gradually at smaller α , while for α closer to 1, depletion is rapid. Figure 6 shows that the latent population peaks later and at higher levels for smaller α , indicating slower progression to the infectious stage. In Figure 7, infectious cases peak later and at reduced amplitudes when α is small, suggesting mitigated short-term outbreak intensity but extended infectious periods. Finally, Figure 8 demonstrates that recovery rates are also α -dependent—lower α delays the accumulation of recovered individuals, while higher α accelerates convergence to the disease-free state. Overall, fractional-order effects captured through varying α highlight the importance of memory in epidemic dynamics, influencing both the timing and magnitude of disease spread. These findings underscore the potential of fractional-order numerical schemes for informing public health strategies, particularly in contexts where disease spread is influenced by history-dependent transmission dynamics. Future work could extend the current framework by adding age structure, waning immunity and targeted vaccination parameters to enhance forecasting for diphtheria and other vaccine-preventable diseases in displaced populations.

Conflict of interest

The authors hereby declare that there is no conflict of interest in the publication of this paper.

Funding

There are no funders to report for this submission.

Author's contributions

M.N.R.-conceptualization, methodology, software, validation, formal analysis, investigation, writing-original draft, and writing-review & editing. M.A.K.-validation, investigation, software, and writing-review & editing. V.C.-validation, formal analysis, and writing-review & editing. M.A.-validation, writing-review & editing. All authors have read and approved the final version of the manuscript.

Acknowledgments

The authors deeply appreciate the reviewers for their helpful and constructive suggestions, which can help further improve this paper.

Availability of data and materials

All data that support the findings of this study are included within the article. The epidemiological data used in this study are derived from publicly available outbreak reports. Due to reporting limitations, the data are available primarily in graphical form. The numerical codes used in this study are available from the corresponding author upon reasonable request.

References

- [1] A.S. Afolabi, M. Miswanto, *Mathematical modeling, optimal control and cost-effectiveness analysis of diphtheria transmission dynamics*, Jamb. J. Biomath. **6(2)** (2025) 88–108.
- [2] Z. Afzal, M. Alshehri, *Fractional-order SIR model for ADHD as a neurobiological and genetic disorder*, Sci. Rep. **15(1)** (2025) 22992.
- [3] A.A. Akhi, F. Tasnim, S. Akter, M. Kamrujjaman, *A mathematical model of a diphtheria outbreak in Rohingya settlement in Bangladesh*, J. Mahani Math. Res. **12(2)** (2023) 547–63.
- [4] N.A. Alshammari, N.S. Alharthi, A. Mohammed Saeed, A. Khan, A.H. Ganie, *Numerical solutions of a fractional order SEIR epidemic model of measles under Caputo fractional derivative*, PloS One **20(5)** (2025) e0321089.

- [5] H.M. Baskonus, H. Bulut, *On the numerical solutions of some fractional ordinary differential equations by fractional Adams-Bashforth-Moulton method*, *Open Math.* **13(1)** (2015) 000010151520150052.
- [6] K. Diethelm, N.J. Ford, A.D. Freed, *A predictor-corrector approach for the numerical solution of fractional differential equations*, *Nonlinear Dyn.* **29(1)** (2002) 3–22.
- [7] K. Diethelm, N.J. Ford, A.D. Freed, *Detailed error analysis for a fractional Adams method*, *Numer. Algorithms* **36(1)** (2004) 31–52.
- [8] K. Diethelm, N.J. Ford, *Analysis of fractional differential equations*, *J. Math. Anal. Appl.* **265(2)** (2002) 229–48.
- [9] B. Ghosh, *Fractional order modeling of ecological and epidemiological systems: ambiguities and challenges*, *J. Anal.* **33(1)** (2025) 341–66.
- [10] R. Gorenflo, F. Mainardi, *Fractional calculus: integral and differential equations of fractional order. In fractals and fractional calculus in continuum mechanics*, Springer, Vienna. (1997) 223–276.
- [11] M. Hafez, F. Alshowaikh, B.W. Voon, S. Alkhazaleh, H. Al-Faiz, *Review on recent advances in fractional differentiation and its applications*, *Progr. Fract. Differ. Appl.* **11** (2025) 245–61.
- [12] Y. He, J. Zhao, L. Wang, C. Han, R. Yan, P. Zhu, T. Qian, S. Yu, X. Zhu, W. He, *Epidemiological trends and predictions of urinary tract infections in the global burden of disease study 2021*, *Sci. Rep.* **15(1)** (2025) 4702.
- [13] H.W. Hethcote, *Three basic epidemiological models*, In: Levin, S.A., Hallam, T.G., Gross, L.J. (eds), *Appl. Math. Ecol.* Springer Berlin, Heidelberg, 1989.
- [14] R. Kamadjeu, O. Okunromade, B.B. Lawal, M. Gadanya, S.A. Suwaid, E.C. Blanco, I. Adetifa, E.A. Kelvin, *Diphtheria transmission dynamics-Unveiling generation time and reproduction numbers from the 2022–2023 outbreak in Kano state, Nigeria*, *Infect. Dis. Model.* **10(2)** (2025) 680–90.
- [15] X. Lu, J. Du, M. You, L. Chen, F. Xu, F. Chen, *From crisis to innovation in point-of-care testing: Lessons from the COVID-19 pandemic and future directions*, *TrAC Trends Anal. Chem.* **184** (2025) 118131.
- [16] M. Martcheva, *An Introduction to Mathematical Epidemiology*, Springer, New York, 2015.
- [17] R. Matsuyama, A.R. Akhmetzhanov, A. Endo, H. Lee, T. Yamaguchi, S. Tsuzuki, H. Nishiura, *Uncertainty and sensitivity analysis of the basic reproduction number of diphtheria: a case study of a Rohingya refugee camp in Bangladesh, November–December 2017*, *PeerJ* **6** (2018) e4583.
- [18] J.D. Murray, *Mathematical Biology: I. An Introduction*, Springer Science & Business Media, 2007.
- [19] K.S. Nisar, M. Farman, M. Abdel-Aty, C. Ravichandran, *A review of fractional-order models for plant epidemiology*, *Prog. Fract. Differ. Appl.* **10(3)** (2024) 489–521.

- [20] A. Oname, M. Abbas, A.H. Abdel-Aty, *Assessing the impact of SARS-CoV-2 infection on the dynamics of dengue and HIV via fractional derivatives*, Chaos Solit. Fractals **162** (2022) 112427.
- [21] J.A. Polonsky, M. Ivey, M.K. Mazhar, O. le Polain de Waroux, B. Karo, K. Jalava, S. Vong, A. Baidjoe, J. Diaz, F. Finger, *Epidemiological, clinical, and public health response characteristics of a large outbreak of diphtheria among the Rohingya population in Cox's Bazar, Bangladesh, 2017 to 2019: a retrospective study*, PLoS Med. **18(4)** (2021) e1003587.
- [22] M.N. Raihen, M.M. Ahammed, S. Akter, *Evaluating the impact of seasonal Influenza virus: A comprehensive epidemiological forecast and analysis in Ghana from 2021 to 2023*, Microbes Infect. Dis. **5(2)** (2024) 463–78.
- [23] M.I. Simoy, *Aparicio JP. Ross-Macdonald models: Which one should we use?*, Acta Trop. **207** (2020) 105452.
- [24] World Health Organization (WHO), 2017, *Diphtheria outbreak response update. Cox's Bazar, Bangladesh-update, 2*. Geneva: World Health Organization. accessed 27 December 2017, <https://www.who.int/emergencies/disease-outbreak-news/item/13-december-2017-diphtheria-bangladesh-en>.
- [25] Z. Yaagoub, *Fractional two-strain SVLIR epidemic model with vaccination and quarantine strategies*, Int. J. Dyn. Control **13(2)** (2025) 55.